Bulletin of Earthquake Engineering (2026) 24:10903–10929
https://doi.org/10.1007/s10518-026-02722-3

ORIGINAL ARTICLE

Impact of pounding interaction on the seismic fragility of low-rise adjacent unreinforced masonry buildings

José A. Gallardo[1,2] · **Igor Tomić**[3] · **Nuria C. Palazzi**[2,4] · **Juan C. de la Llera**[1,2] · **Katrin Beyer**[3]

Received: 5 April 2026 / Accepted: 6 October 2026 / Published online: 22 October 2026
© The Author(s), under exclusive licence to Springer Nature B.V. 2026

Abstract
Unreinforced masonry (URM) buildings, prevalent in historic urban centers, often constitute an architectural typology of kinematically coupled clusters, where independent structural units are built in direct adjacency. Despite this, seismic performance assessments typically analyze these buildings as isolated structures, a common practice that overlooks the interaction between neighboring structures, resulting in unrealistic demands and fragility estimates. This research studies this dynamic coupling by modeling three distinct URM building archetypes and assembling them into seven different two- and three-unit clusters to evaluate the influence of building position and differences in strength and stiffness between neighboring structures. Using a three-dimensional equivalent frame approach that captures both in-plane and out-of-plane behavior of masonry walls, fragility curves for each isolated unit were derived from nonlinear response history analyses, using a suite of actual ground motions and following the multiple stripe analysis methodology. Then, fragility curves of the buildings within the clusters were also developed and compared with those of the isolated structural units. Results show a complex, configuration-dependent interaction. While weaker buildings (i.e., lower in-plane stiffness and lower strength capacity) benefit from the support of stronger neighbors, this support renders the stronger units more fragile, an effect that intensifies with increasing stiffness disparity. The collapse sequence is initiated by the most vulnerable unit, regardless of its position within the cluster, which can trigger a progressive collapse that compromises adjacent, otherwise stable, structures. This study provides quantitative evidence that assessing URM buildings in isolation is not only flawed but unconservative. Therefore, the seismic fragility of URM buildings cannot be quantified in isolation; it needs a holistic approach, developing cluster-level models for realistic performance assessments of historic urban centers.

Keywords Masonry · Pounding · Equivalent frame model · Seismic fragility · Seismic performance · Nonlinear response history analysis

Extended author information available on the last page of the article

1 Introduction

Throughout history, earthquakes have had a devastating impact on communities, resulting in numerous fatalities and substantial economic losses (UNDRR 2019). In particular, they have repeatedly highlighted the vulnerability of older structures (Çetin et al. 2023), which consist predominantly of unreinforced masonry (URM) buildings (Tomazevic 1999; D'Ayala and Speranza 2003; Carocci 2012; da Porto et al. 2013; Penna et al. 2014). This construction typology is one of the most ancient and globally widespread (Shabani et al. 2021), and its prevalence in historic urban centers within high-seismicity regions, such as parts of Europe (Carocci 2012; Bernardini et al. 2019; Pnevmatikos et al. 2020; Ruggieri et al. 2023) and South America (D'Ayala and Benzoni 2012; Salazar et al. 2020; Palazzi et al. 2023; Baquedano-Juliá et al. 2024), raises significant concerns about the potential consequences of future earthquakes. The historical record of seismic damage substantiates these concerns; for instance, the historical center of Santiago, Chile, suffered severe damage during the 1985 Algarrobo and 2010 Maule earthquakes (D'Ayala and Benzoni 2012; Palazzi et al. 2023). Similar widespread damage to URM building stock has been observed in Italian earthquakes, such as L'Aquila 2009 and Central Italy 2016 (Carocci 2012; Indirli et al. 2013; Fiorentino et al. 2018), as well as in Croatia during the 2020 earthquakes (Atalić et al. 2021, 2023; Uroš et al. 2024), among others (Shrestha and Hao 2018; Ismail and Khattak 2019). Therefore, understanding the factors that govern the seismic performance of these buildings is an essential first step toward improving seismic risk management and mitigating future losses in these vulnerable and historically valuable urban centers.

The seismic behavior of a single URM building is, by itself, very complex. Factors such as material heterogeneity, the quality of connections between orthogonal walls, the interaction between walls and flexible timber floors, and the inherent brittle response of masonry elements lead to highly nonlinear behaviors that are challenging to simulate numerically. This complexity is further magnified by an architectural typology typical in historic urban centers where buildings are constructed in direct adjacency to pre-existing ones, often with no separation gaps (i.e., clusters) and sometimes even sharing load-bearing walls (i.e., aggregates). This arrangement ensures that each structural unit interacts dynamically with its neighbors, creating a large and structurally interdependent system. Consequently, assessing a URM building that is part of a cluster or an aggregate as an isolated structure, an assumption typical in vulnerability and risk assessments, is a flawed practice that leads to unrealistic estimates of its demands and inaccurate risk quantification (Tomić et al. 2024a). While the need to understand this inter-building interaction has gained increasing attention over the last decade, progress has been limited by the lack of experimental data, primarily due to the high costs associated with conducting dynamic tests on entire multi-building systems. This, in turn, has led to difficulties in calibrating numerical models that simulate the interaction between the units and, ultimately, to a lack of clear guidelines and provisions in building codes (Tomić and Beyer 2024).

Recently, two large-scale experimental campaigns have provided crucial insights into the inter-building interaction. The first, conducted by Senaldi et al. (2020) and Guerrini et al. (2019), tested a half-scale specimen consisting of two three-story stone masonry units connected with interlocking stones and flexible timber floors. A second campaign, led by Tomić et al. (2024a), tested a half-scale masonry aggregate comprising two adjacent units built with double-leaf undressed stone masonry and timber floors of differing orientations. The

units had different heights to represent the irregular geometries typical of historic urban centers. The results showed significant interaction between the units in both the longitudinal and transverse directions, which influenced the observed damage mechanisms and highlighted the role of inter-building interaction in the overall system response. This latter test was accompanied by a blind prediction competition (Tomić et al. 2024b) where participants from academia and practice applied a wide spectrum of modeling approaches (AlShawa et al. 2024; Aşıkoğlu et al. 2024; Bianchini et al. 2024; Gagliardo et al. 2024; Galvez et al. 2024; Ramaglia et al. 2024; Malomo and DeJong 2024). The results revealed substantial variability among predictions, reflecting the broader modeling difficulties inherent to URM buildings and, by extension, interacting clusters and aggregates. Furthermore, they indicated that explicitly accounting for the interaction between individual units is crucial for accurately capturing the multi-unit system's dynamic behavior.

In response to the complexity of modeling the full multi-unit system, various strategies have been proposed to facilitate vulnerability assessments. A widely used procedure is based on limit state analysis and failure mechanisms of the façades (D'Ayala 2013), which was calibrated with empirical fragility curves (Palazzi et al. 2023). A simplified method based on vulnerability forms utilizes the physical and geometrical characteristics of the studied building and its adjacent structural units (Formisano et al. 2015). These assessment strategies offer practical tools for a fast risk assessment, especially for large portfolios where time and resources are limited. Nevertheless, when aiming to perform more detailed analyses that explicitly account for epistemic and aleatory uncertainties, the preferred modeling approach for URM buildings is the equivalent frame model (EFM). This approach simplifies the structural representation by treating each masonry component (i.e., piers and spandrels) as a single nonlinear element, capable of simulating the global behavior of the component with relatively low computational cost (Quagliarini et al. 2017). The computational efficiency of the EFM makes it an ideal tool for systematically addressing specific aspects of the inter-building behavior. However, despite significant research efforts employing both simplified methods (Formisano et al. 2015; Formisano and Massimilla 2018) and detailed modeling (Bernardini et al. 2019, Greco et al. 2020; Angiolilli et al. 2021, 2023; Di Trapani et al. 2024; Malomo and DeJong 2024) to study the inter-building pounding, a comprehensive understanding of the interactions between adjacent buildings, particularly those with differing strengths and stiffnesses, remains limited.

While existing research has identified critical factors influencing the seismic behavior of URM buildings within clusters (Malomo and DeJong 2024), a systematic study isolating the effect of a building's position and the relative strength and stiffnesses of its neighboring structures remains a key research gap. Therefore, the novelty of this research lies in the quantitative assessment of inter-building pounding and its direct impact on the seismic fragility of unreinforced masonry buildings. To achieve this, three distinct structural archetypes inspired by the buildings of the Yungay neighborhood in Santiago, Chile, are developed and modeled using the EFM proposed by Vanin et al. (2020b). A key feature of this formulation is the explicit consideration of the out-of-plane (OOP) behavior of masonry walls and its coupling with the in-plane (IP) response, aspects that have often been neglected in previous analyses. Fragility curves are generated for each structural unit using Multiple Stripe Analyses (MSA) and employing a suite of ground motion (GM) records representative of the local seismic hazard. By assembling the archetypes into various two- and three-unit clusters, this research systematically investigates how structural interaction and position impact the

failure mechanisms of each structural unit, allowing for a direct comparison between the fragility of a unit in a cluster and in isolation. The findings reveal a complex, configuration-dependent pounding effect: the seismic performance of weaker buildings is enhanced by stronger neighbors, but this support often comes at the cost of increasing the fragility of the stronger unit. Furthermore, the results show that the collapse sequence is initiated by the most vulnerable unit, regardless of its position, which can trigger a progressive failure that compromises adjacent, otherwise stable, structures.

2 Description of structural archetypes and cluster configurations

To investigate how cluster configuration modifies the seismic fragility of URM buildings, a virtual experiment was designed based on a set of representative structural archetypes. These archetypes were developed from an analysis of 115 buildings surveyed in the Yungay quarter, a heritage neighborhood in the historic center of Santiago de Chile. The survey collected data on geometric, morphological, and material features, which enabled the definition of the archetypal models (i.e., simplified mechanical representations that capture the behavior of a class of buildings for which only partial or uncertain information is available, as described in Ruggieri et al. 2023). The selected archetypes correspond to two-story unreinforced brick masonry buildings, representative of the "Santiago Poniente" construction culture (Jorquera-Silva 2017). This typology emerged in the nineteenth century when European architects and engineers were invited by President Manuel Bulnes to modernize the city's image, replacing the austerity of traditional colonial architecture.

This study focuses specifically on the Classicist and Variant (Cl&Va) typology (Palazzi et al. 2023), characterized by urban cluster built simultaneously using homogeneous construction techniques, primarily unreinforced brick masonry. These structures typically feature elongated floor plans, with façades ranging from 6 to 12 m in width, an overall façade height of approximately 8 to 9 m, and transverse partition walls extending 12 to 60 m in length. The façades exhibit a regular and vertically aligned distribution of door and window openings. Roofs are gabled and built with oak king-post trusses, complemented by flat timber ceilings. Structurally, Cl&Va buildings comprise thick external brick walls (0.4–0.6 m), with lighter internal partitions made of timber-frame systems (tabique). While strong orthogonal wall connections allow for integrated seismic box behavior, Cl&Va buildings typically lack traditional seismic-resistant features such as steel ties, buttresses, or reinforced ring beams at the top of façades (Palazzi et al. 2023). This typology has been identified as one of the most seismically vulnerable configurations within the historic urban fabric of the Yungay neighborhood, especially in two-story structures (Muñoz et al. 2025). Consequently, this typology provides a critical structural archetype for investigating how inter-building pounding influences the seismic fragility of historic URM buildings.

To isolate the pounding effect and provide general insights into its impact on the seismic behavior of URM buildings, specific architectural features of the Yungay neighborhood, such as roof overhangs (antetechos), internal dividing walls built with mixed timber-masonry technique (tabique), and beveled corners (ochavos) (Palazzi et al. 2023), were omitted from the archetypes. While these elements are known to be vulnerable and can influence local damage patterns, they introduce additional layers of complexity to the numerical modeling. Moreover, their exclusion allows for a more fundamental analysis of the global dynamic

interaction between adjacent structural units, which is the focus of this study. Furthermore, since the analysis is based on idealized archetypes, possible alterations or modifications made to the original structures after their construction (e.g., partial demolitions, structural reinforcements, or irregular openings) were also excluded.

2.1 Structural units archetypes

Three structural archetypes were designed for this study to represent buildings with varying characteristics, specifically stiffness and strength capacity, commonly found in historic urban centers where building footprints and façades vary significantly. The primary variable distinguishing the units is their façade length (number of piers). Because the mechanical properties are kept constant to minimize sources of uncertainty, it is this variation in façade length that governs the differences in their strength and stiffness, despite some other geometric variations. Hereafter, the archetypes are referred to as Unit A, Unit B, and Unit C, where Unit A is the shortest and most flexible, whereas Unit C is the longest and stiffest (see Fig. 1).

All three units share common structural and geometric attributes consistent with the Cl&Va typology of the Yungay neighborhood. They are two-story structures with a uniform story height of 4.0 m, resulting in a total building height of 8.00 m, and a consistent masonry wall thickness of 0.40 m, typical of URM walls in this region. The parameters defining the regularly distributed openings were also selected to be representative of the historic urban fabric. All façades have door openings of 3.00 m by 1.20 m (height by width), window openings of 2.00 m by 1.20 m, and a uniform distance of 1.00 m from the building edges to the first opening. For Unit A, the longitudinal spacing between openings is 1.80 m, resulting in a total length of 6.20 m. For Units B and C, this spacing is 1.50 m, corresponding to total lengths of 8.60 m and 11.30 m, respectively. Photographs of representative buildings along the archetypal façades are presented in Fig. 1. Finally, all three units can be classified as URML (Unreinforced Masonry Bearing Walls, Low-Rise) according to FEMA (2020).

The structural units are designed to be symmetrical to avoid any potential torsional effects during seismic events. To achieve this symmetry, the back façade mirrors the front façade, while solid, regular orthogonal walls connect the façades at the borders, enclosing the building (as visualized in the numerical models in Fig. 2a–c). Good interlocking is assumed between perpendicular walls (Palazzi et al. 2023). The floors are constructed of timber beams and planks, using oak as the representative species for the region. The timber beams for the floor have a cross-section of 9.0 cm by 14.5 cm, while the roof beams are 4.5 cm by 14.5 cm. The beams are spaced at 1.4 m intervals. To complete the floor system, two layers of timber planks, each 2.0 cm thick, are nailed onto the top of the beams, creating a flexible diaphragm with a total thickness of 4.0 cm. As a direct consequence of their different geometries, the units exhibit distinct dynamic properties, with first translational periods in the longitudinal direction of 0.19 s (Unit A), 0.17 s (Unit B), and 0.14 s (Unit C), reflecting the increasing stiffness due to the longer façade length. A summary of the primary geometric and dynamic parameters defining each archetype is provided in Table 1.



Fig. 1 Overview of the case study area and the selected archetypes: (**a**) aerial view of urban blocks in the Yungay quarter, composed of CI&Va buildings (©2025 Google maps); (**b**) photographs showing the front façades of representative buildings; and (**c**) schematic elevation of the front façades for the structural archetypes: Unit A, Unit B, and Unit C

2.2 Cluster configurations

This research focuses on the typology known as *row housing* (Formisano and Massimilla 2018), which consists of a series of structural units arranged in a line, generally parallel to the streets. Clusters comprising two and three structural units are generated by assembling the archetypes adjacent to one another with zero separation gap.

To account for various configurations, several structural unit combinations are considered. Since each structural unit is assumed to be a self-supporting building, there are no mechanical connections between the adjacent walls of different units. Therefore, the inter-

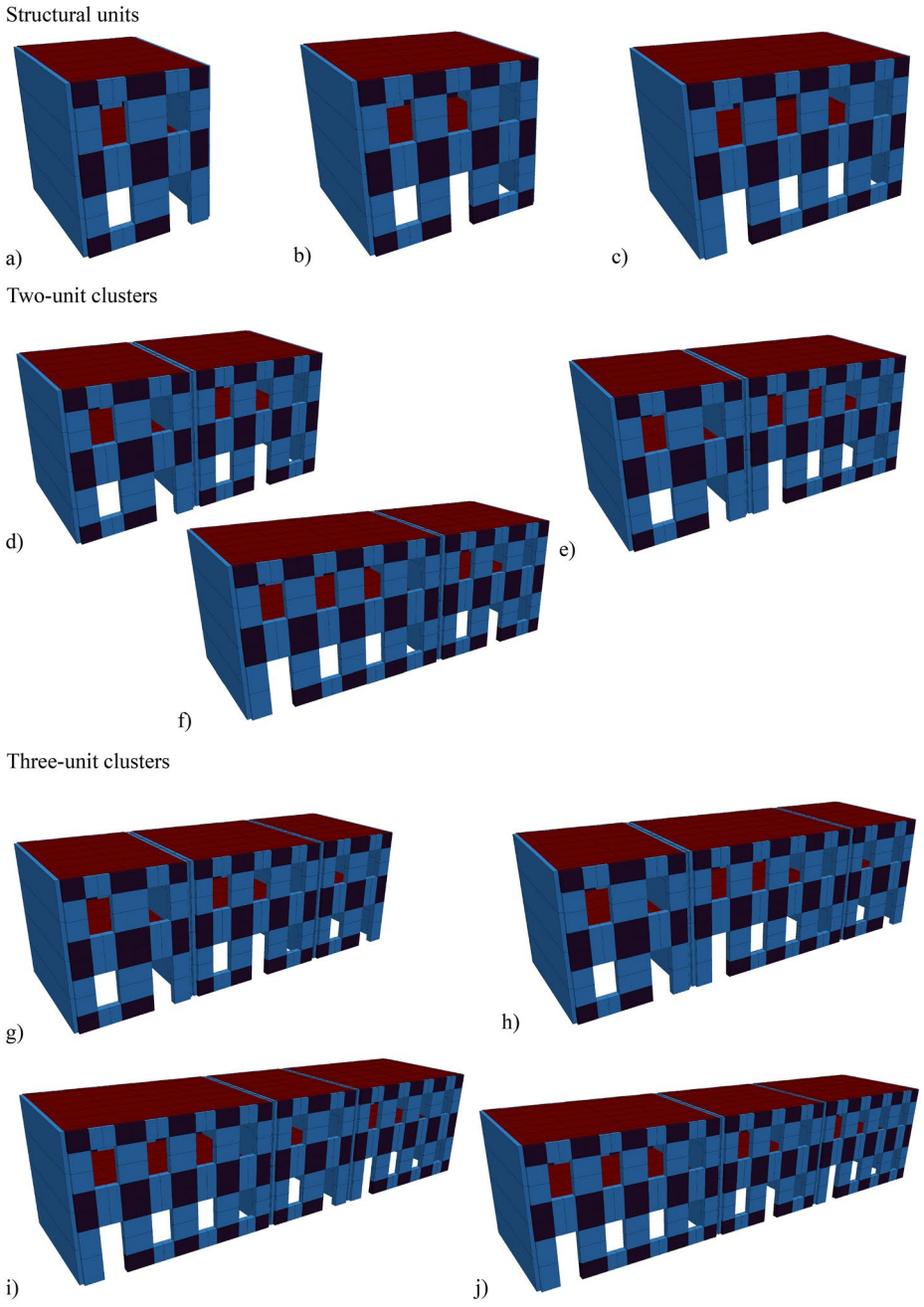


Fig. 2 Schematic views of the numerical models for individual structural units and cluster configurations. Structural units: (**a**) Unit A, (**b**) Unit B, and (**c**) Unit **C.** Two-unit clusters: (**d**) AG_{AB}, (**e**) AG_{AC}, and (**f**) AG_{CB}. Three-unit clusters: (**g**) AG_{ABA}, (**h**) AG_{ACA}, (**i**) AG_{CAC}, and (**j**) AG_{CBC}. Models were visualized in ParaView utilizing a custom python module developed by the authors

Table 1 Summary of geometric and dynamic properties for the structural archetypes. The fundamental periods correspond to the longitudinal translation (parallel to the façades)

Archetype	Total length [m]	Opening spacing [m]	First translational period [s]
Unit A	6.20	1.80	0.19
Unit B	8.60	1.50	0.17
Unit C	11.30	1.50	0.14

action between adjacent buildings is driven solely by pounding resulting from differential displacements and out-of-phase dynamic responses.

Three two-unit clusters were generated for this study, representing distinct pairwise combinations of the three archetypes. The nomenclature used is AG_{xy}, where x and y denote the unit names from left to right. The three two-unit configurations considered are AG_{AB}, AG_{AC}, and AG_{CB}. Similarly, four three-unit clusters were generated, following the extended nomenclature AG_{xyz}, where x, y, and z represent the sequential unit names from left to right. The four three-unit configurations analyzed are AG_{ABA}, AG_{ACA}, AG_{CAC}, and AG_{CBC}. These combinations were specifically selected to evaluate key scenarios, including the effect of a stronger central building, the confinement of a weaker building between two stronger ones, and the impact of disparities in stiffness and strength capacity between the corner and central buildings. Schematic views of the structural models and cluster configurations are presented in Fig. 2. In total, ten numerical models were analyzed: the three isolated structural units and the seven cluster configurations described above. It is worth noting that increasing the number of units in a cluster substantially increases the computational burden; therefore, the scope of this research was limited to clusters comprising a maximum of three units.

3 Numerical modeling

Three-dimensional models of both the structural archetypes and the cluster configurations described in the previous section were developed using the open-source software OpenSees (McKenna et al. 2000). Structural units were represented using the EFM approach, which accurately captures the phenomenological behavior of masonry walls at a structural element level (i.e., piers and spandrels). This simplified numerical modeling strategy is widely adopted due to its limited computational burden and its effectiveness in predicting the global seismic response of masonry buildings (D'Altri et al. 2020). The following subsections provide a detailed explanation of the numerical formulation used for all elements and their respective connections. Fig. 3 presents a graphical representation of the numerical modeling approaches, while Table 2 shows the values of all required parameters. It is worth reiterating that internal partition walls (tabiques) were not included in the numerical models.

3.1 Masonry elements

All masonry elements are modeled using the EFM approach, where each façade is discretized into spandrels and piers, which are rigidly connected. Piers are the vertical elements supporting vertical and horizontal loads, while spandrels are the horizontal elements that couple the piers, commonly located above and below door and window openings. The connection zones between the piers and the spandrels are assumed to be rigid panels, as

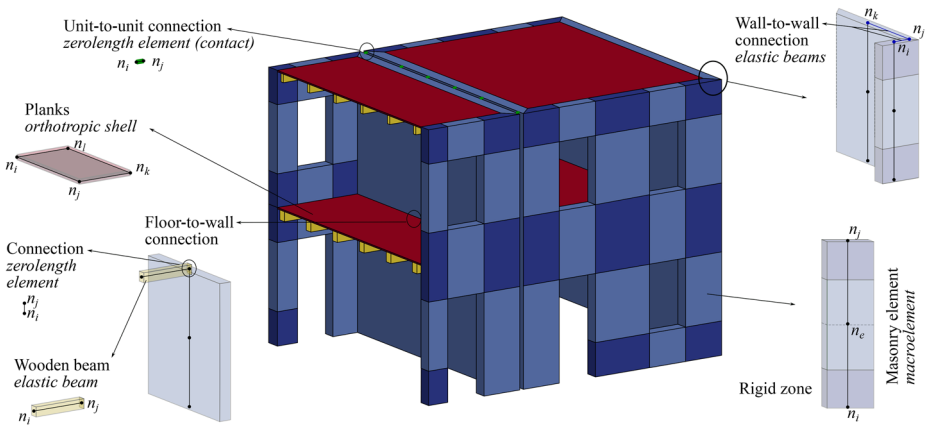


Fig. 3 Schematic representation of the numerical modeling approach: EFM idealization for unreinforced masonry walls (piers and spandrels), wall-to-wall connections, timber floors (beams and planks), floor-to-wall connections, and the contact interfaces simulating inter-building interaction

Table 2 Summary of material properties and interface parameters adopted for the masonry walls, timber elements, and connections in the numerical model

Material parameter	Reference	Value
Masonry walls		
Peak compressive strength, f_c [MPa]	Experimental test	4.20
Elasticity modulus, E[MPa]	INN (2020)	$600 f_c$
Shear modulus, G[MPa]	INN (2020)	$E/4$
Friction coefficient, μ	Vanin et al. (2020a)	0.23
Cohesion, c[MPa]	Experimental test	0.28
Shear deformation parameter, G_c[-]	Vanin et al. (2020b)	6.0
Drift at 20% force capacity loss, s_ξ [%]	Vanin et al. (2020a)	0.25
Residual friction coefficient, μ_R[-]	Vanin et al. (2020b)	$\mu/3$
Timber elements		
Elasticity modulus (GD), $E_{p,g}$ [MPa]	INN (2020)	9100
Elasticity modulus (TGD), $E_{p,t}$ [MPa]	Ross (2010)	$0.082E_{p,g}$
Shear modulus (GD), $G_{p,g}$[MPa]	Ross (2010)	$0.089E_{p,g}$
Shear modulus (TGD), $G_{p,t}$[MPa]	Ross (2010)	$0.081E_{p,g}$
Equivalent shear stiffness, G_{eq} [MPa]	Brignola et al. (2008)	1.364
Poisson's ratio, μ_p[-]	Ross (2010)	0.35
Specific gravity, ρ_p[-]	Ross (2010)	0.58
Floor-to-wall connections		
Friction coefficient, μ_{wf}[-]	Almeida et al. (2020)	0.70
Unit-to-Unit connections		
Maximum expected indentation, δ_{me}[cm]	Hughes and Mosqueda (2020)	0.10

empirical evidence shows that these areas typically remain undamaged during seismic actions (Quagliarini et al. 2017). This assumption is suitable for the structural archetypes in this study, given their highly regular, vertically aligned openings and consistent pier and spandrel dimensions. The mechanical response of the spandrels and piers was simulated using the three-node macro-element proposed by Vanin et al. (2020b). This formulation captures both the in-plane (shear and flexure) and the out-of-plane responses of these components and has been shown to accurately predict the performance of masonry buildings during earthquakes (Vanin et al. 2020a; Tomić et al. 2021). Notably, this formulation captures only the global response rather than localized damage patterns (e.g., combined OOP bending or the formation of diagonal hinges). The interested reader can refer to Vanin et al. (2020b) for a detailed explanation of the capabilities and limitations of this formulation.

The material parameters are consistent across all three structural archetypes. The maximum compressive strength of the masonry (f_c) and cohesion (c) were obtained from experimental tests on samples extracted from buildings in the Yungay neighborhood, yielding values of 4.20 MPa and 0.28 MPa, respectively. Following the provisions of Chilean Standards (INN 2020), the modulus of elasticity (E) and shear modulus (G) of the masonry were computed as $E = 600 f_c$ and $G = 0.25E$. The values for the friction coefficient (μ) and drift at a 20% loss in force capacity (s_ξ) were taken as 0.23 and 0.25%, respectively; these values are calibrated for this specific formulation (Vanin et al. 2020a). The shear deformation parameter (G_c) was set to 6.0, and the residual friction coefficient (μ_R) was computed as $\mu_R = \mu/3$, as suggested by Vanin et al. (2020b). In the *OpenSees* formulation, a distinction is made between spandrels and piers by using the flags *-spandrel* and *-pier*, respectively. Further details on these element implementations can be found in Vanin et al. (2020b). Geometrical non-linearity was considered for the piers by using the flag *-pDelta*. Additionally, a secant-stiffness proportional damping model was adopted for the piers to avoid overdamping the out-of-plane behavior.

3.2 Wall-to-wall connection

All wall-to-wall connections within a structural unit are assumed to be of good quality due to the adequate interlocking of the bricks. Therefore, the intersection between orthogonal walls is modeled using an elastic beam element that connects the walls, distributes vertical loads (i.e., capturing the flange effect), and restricts differential lateral displacements. Following the methodology presented by Cattari et al. (2023), the connecting beam is assigned a large axial and flexural stiffness, whereas its shear stiffness is calibrated according to the connected wall properties. The shear stiffness is controlled by the dimensionless parameter ω, which depends on the geometrical and mechanical characteristics of the connected walls (Cattari et al. 2023), computed as

$$\omega = \frac{K_z h^2}{E_W A_W} \left(\frac{1+\zeta}{\zeta} + \frac{12 d^2}{l_W^2} \right), \tag{1}$$

where K_z is the shear stiffness of the connection; h is the height of the masonry walls; A_W, E_W, and J_W are the cross-sectional area, modulus of elasticity, and moment of inertia of the web wall, respectively; $\zeta = (E_F A_F)/(E_W A_W)$, where A_F and E_F are the cross-sectional area

and the modulus of elasticity of the flange wall, respectively; d is the distance between the centroid of the web wall and the flange wall; and l_W is the length of the web wall.

The parameter ω can be calibrated to represent different connection qualities. For example, a value of 100 represents a rigid connection, whereas a value of 1.0 represents an intermediate-to-poor connection. For this study, a value of $\omega = 5$ was adopted to model a good-quality, yet not perfectly rigid, connection. The properties of the equivalent beam connecting the walls are computed to develop the same shear stiffness as that of the connection, determined as

$$K_z h = \frac{5 G_W A_B}{6 l_B}, \tag{2}$$

where G_W is the shear modulus of the web wall; and l_B and A_B are the length and cross-sectional area of the equivalent beam, respectively. Note that this formulation assumes that the material of the equivalent beam is the same as that of the web wall. Consequently, no additional parameters are needed to calibrate the wall-to-wall connections. However, it is worth noting the limitations of this formulation. Since the connection is modeled elastically, it only represents stiffness and does not account for strength capacity. Consequently, the model cannot reproduce rigid-plastic disconnecting mechanisms, the physical separation between orthogonal walls, or the propagation of cracks into adjoining walls if the connection possesses higher shear strength than the masonry.

3.3 Timber floors

Timber beams and planks for the floor and roof are modeled independently. The beams are modeled using elastic frame elements embedded in the supporting walls. The planks, which are supported by the beams and attached with nails, are modeled using shell elements based on the first-order shear deformation plate theory, following the implementation presented in Reddy (2014), Section 7.7. An orthotropic material model is assumed to account for the different stiffnesses along and across the grain. Material properties representing of oak are used, with a modulus of elasticity of 9100 MPa in the grain direction (INN 2020) and a Poisson's ratio of 0.35. The remaining properties were taken from Ross (2010) and are summarized in Table 2.

The in-plane shear stiffness of the planks is computed using a method previously proposed for this floor typology (Brignola et al. 2008). This method considers that the total shear deformation of the diaphragm depends on the combined contribution of the flexural and shear deformation of the planks, plus the deformation due to the rigid rotation of individual planks resulting from nail slip. For the diaphragm stiffness calculation, it is assumed that nails with a 4 mm diameter are spaced 14 cm apart on each side of the planks, which are 30 cm in width. Finally, an additional mass of 50 kg/m^2 is added to the first floor to account for internal partitioning walls and furniture. It should be noted that while the internal transverse partition walls (tabiques) are excluded from the lateral resisting system in the numerical model, they are assumed to provide intermediate vertical support to the longitudinal floor beams. This effectively reduces the bending spans to realistic distances for the timber elements. Consequently, the gravity loads and floor mass are distributed to the main

load-bearing façades and the assumed intermediate supports based on their tributary areas, ensuring a realistic representation of the structural mass distribution.

3.4 Floor-to-wall connection

The connections between the timber beams and the supporting masonry walls are modeled by representing the beams as embedded into the walls without explicit mechanical connectors. It is assumed that there are no gaps between the beams and the lateral surfaces of the wall pockets. Therefore, the stiffness of the connection element is assigned a sufficiently large value in the vertical and transverse directions to prevent differential movements. Conversely, relative displacement is allowed along the longitudinal axis of the beam, and the resulting resisting force is governed by friction between the elements. Consequently, a friction coefficient (μ_{wf}) of 0.7 is adopted, a value consistent with those reported for similar timber-masonry interfaces (Almeida et al. 2020).

3.5 Unit-to-unit connection

The interaction between adjacent, separate structural units is modeled using a nonlinear elastic element to simulate the effects of seismic pounding. This element exhibits a dual behavior: it has negligible tensile stiffness (set to a near-zero value to avoid numerical instability), which allows for the unrestricted separation of the buildings when the gap between them increases; conversely, when the units move towards each other and the gap closes, the element provides an elastic compressive stiffness to represent the pounding force. This approach was chosen because previous research has demonstrated that this type of simplified contact model can produce results with an accuracy comparable to that of more sophisticated and computationally intensive models (Hughes and Mosqueda 2020).

The effective compressive stiffness (k_{eff}) is computed as

$$k_{eff} = k_h \sqrt{\delta_{me}}, \tag{3}$$

where δ_{me} is the maximum expected indentation, which is a heuristic parameter set to 0.1 cm for this model as suggested by Hughes and Mosqueda (2020). The Hertz stiffness, k_h, is based on Goldsmith's formulation (Goldsmith 1960) for colliding bodies (this was originally developed for an impact between two colliding spheres) and is given by

$$k_h = \frac{4}{3\left[\left(\frac{1-\nu_1^2}{E_1}\right)+\left(\frac{1-\nu_2^2}{E_2}\right)\right]\sqrt{\left(\frac{4\pi}{V_1}\right)^{1/3}+\left(\frac{4\pi}{V_2}\right)^{1/3}}}, \tag{4}$$

where E_1, E_2 and ν_1, ν_2 are the moduli of elasticity and Poisson's ratios of the adjacent masonry walls, respectively. The parameters V_1 and V_2 represent the effective volumes of the colliding wall segments. To compute these volumes at different elevations, the wall was divided into tributary areas according to the vertical spacing of the impact nodes. Specifically, the discrete contact points between the adjacent structures were established at the story levels and at the mid-height of each story. For the calculation of the tributary areas, a vertical height of 2 m was considered for each contact point, with the exception of the con-

tact on the roof, which assumed a tributary height of 1 m. The volume V for each segment was assumed to be the respective tributary area multiplied by the wall thickness. Finally, to ensure an accurate distribution of forces across the interface, the total effective stiffness k_{eff} computed for a specific story height was divided equally by the number of connecting elements (nodes) located at that same elevation.

4 Seismic performance assessment

The seismic performance of the structural units, both in isolation and within the clusters, was evaluated through NonLinear Response History Analyses (NRHAs). The results from these dynamic analyses were subsequently used to derive seismic fragility curves. Because the primary objective of this study is to quantify the pounding effect, all analyses were performed exclusively in the longitudinal direction of the structural units (i.e., parallel to the front façade), as this is the primary axis along which seismic pounding interactions occur.

4.1 NonLinear response history analysis

For the NRHAs, ten sets of 20 GM records were selected, with each set corresponding to a specific intensity level representing return periods of 50, 100, 200, 500, 750, 1000, 1500, 2000, 2500, and 3000 years. This procedure was adopted to compute fragility curves using the MSA method. The GM selection process comprised three steps: the computation of a site-specific hazard curve, the development of the conditional spectra for each intensity level, and the selection of GM records matching each target spectrum.

The seismic hazard curve was computed for the Yungay neighborhood (33°26′27″S, 70°42′00″W) using the SeismicHazard platform (Candia et al. 2019), assuming a soil type B (characterized by a V_{S30} ranging between 500 m/s and 900 m/s) according to the Chilean standard (INN 1996). Subsequently, conditional spectra were computed for the ten selected return periods. Finally, for each target spectrum, 20 records were chosen from the SIBER-RISK database (Castro et al. 2022) using the algorithm proposed by Jayaram et al. (2011). For the selection process, the two horizontal components of each seismic record were assumed to be independent. The spectral acceleration at the first translation period in the longitudinal direction of the medium-sized structural unit (T_{cond} = 0.17s, the periods of the three structural units ranged from 0.14 to 0.19 s) was used as the conditioning intensity measure (IM).

Fig. 4 presents the results of this selection process, illustrating the individual and mean response spectra for the selected GM records for three representative return periods (100, 500, and 2500 years).

4.2 Fragility analysis

The seismic fragility of each structural unit is expressed using a lognormal cumulative distribution function (CDF), which describes the probability of reaching or exceeding a specific damage state (in this case, collapse) conditionally upon a given level of GM intensity. This function is mathematically defined as

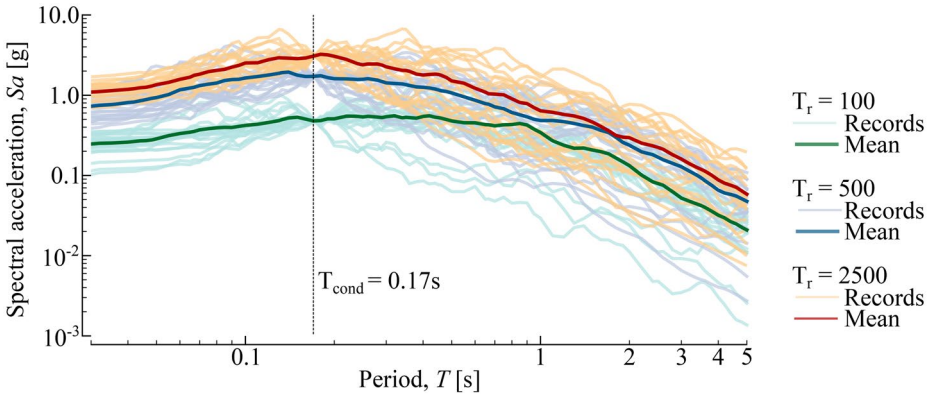


Fig. 4 Individual and mean response spectra of the selected GM records for return periods of 100, 500, and 2500 years

$$P(C|IM = x) = \Phi\left(\frac{\ln(x/\theta)}{\beta}\right) \tag{5}$$

where $P(C|IM = x)$ is the probability that a GM with an intensity level of x will cause the structure to collapse; $\Phi(\bullet)$ is the standard normal CDF; θ is the median of the fragility function (i.e., the IM level corresponding to a 50% probability of collapse); and β is the standard deviation of $\ln(IM)$ (commonly referred to as the dispersion of IM).

The parameters of the fragility function, θ and β, are estimated by fitting the lognormal CDF to the discrete data points obtained from the MSA. For each intensity level, or "stripe," an empirical probability of collapse is calculated as the ratio of the number of simulations resulting in collapse to the total number of GM records applied at that stripe. The fitting process to determine the optimal θ and β values is performed using the maximum likelihood estimation, following the procedure outlined by Baker (2015).

In this study, the collapse of a structural unit is defined as the failure of at least 50% of the piers in any given story, evaluated independently in each orthogonal direction. Individual pier failure itself is defined by IP drift or OOP displacement limits. For IP behavior, failure is triggered when the drift exceeds a limit of 0.9% for shear drift or 1.2% for flexural drift. The macro-element formulation allows for independent tracking of the drift associated with shear and flexural behavior. For OOP failure, pier failure is assumed to occur when a pier reaches its maximum transverse displacement capacity, leading to a loss of stability. These limit states are consistent with values previously adopted in the literature for similar masonry buildings (Tomić et al. 2021).

5 Results

This section presents the outcomes of the numerical analyses performed on both the isolated structural units and the clusters. The results of the NRHAs are first presented for the individual structural units, followed by an evaluation of their performance when interacting within the clusters.

5.1 Isolated structural units

The initial analyses focused on characterizing the fundamental properties of the three isolated structural archetypes using the results of the NRHAs. These aimed to understand the features controlling the seismic behavior of these buildings, quantify their seismic fragility, and determine their most probable failure mechanisms.

Fig. 5 illustrates the relationship between the total base shear, normalized by the seismic weight (F_s/W), and the total drift (δ) for the three structural units. The plots capture the structural response at the instants of peak base shear, peak rooftop displacement, and the envelope of these peak responses. Unit C shows the highest stiffness and strength capacity, reaching a higher shear force for a given level of drift. Conversely, Unit A and Unit B exhibit a more flexible behavior, accommodating larger drifts at lower shear force levels. It is important to note that the response states at the instants of peak base shear and peak rooftop displacement do not coincide. This discrepancy provides a critical insight for understanding the complex dynamic behavior of masonry buildings, as it is a consequence of the local vibration modes superimposing onto the global translational response. The numerical model used for simulating the behavior of masonry walls accounts for the OOP response, which is responsible for this local behavior. During a seismic event, individual walls vibrate in the OOP direction, each with its characteristic period and phase, which differ from the global translational response of the unit. This behavior is explained by the vibration modes of the structural units, which exhibit distinct local OOP frequencies that do not coincide with the global translational modes. Consequently, these local modes significantly affect the overall dynamic response, highlighting that the building does not behave as a simple element and emphasizing the necessity of using advanced models capable of capturing these complex three-dimensional effects.

Fig. 6 presents the seismic fragility curves for the three structural units (whose parameter values are summarized in Table 3), using the spectral acceleration at the conditioning period $Sa(T_{cond})$, and peak ground acceleration (PGA) as intensity measures. The use of PGA is included primarily for comparison purposes, as it is a widely adopted IM in previous literature. The results are consistent with the previous analysis, showing that Unit A is the most fragile, followed by Unit B and Unit C, respectively. Based on the $Sa(T_{cond})$ as the IM, the ratios of the median collapse capacity (θ) of Unit C and Unit B relative to Unit A are 2.59 and 1.33, respectively. However, the dispersion values (β) of the curves are quite similar, ranging from 0.71 to 0.82. Regarding the fragility curves that use PGA as the IM, the results are consistent with findings from the literature.

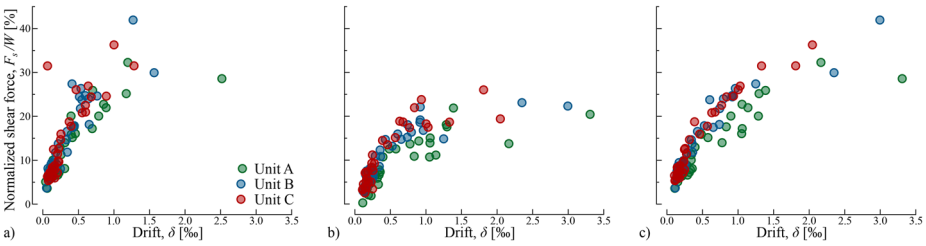


Fig. 5 Normalized base shear (F_s/W) versus total drift (δ) for the three structural units. The data points represent: (**a**) the response at the instant of maximum base shear, (**b**) the response at the instant of maximum rooftop displacement, and (**c**) the peak base shear versus the peak roof displacement

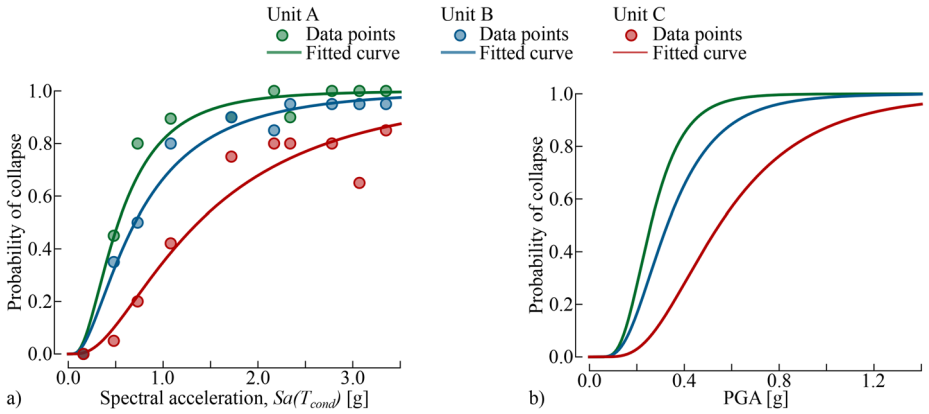


Fig. 6 Fragility functions for collapse of the structural units considering (**a**) The spectral acceleration at the conditioned period, $Sa\,(T_{cond})$, and b) the peak ground acceleration (PGA) as intensity measures

Table 3 Parameter values for the fragility curves of the three structural units, using $Sa(T_{cond})$ and PGA as IM

	$Sa\,(T_{cond})$ [g]		PGA [g]	
Structure	$\hat{\theta}$	$\hat{\beta}$	$\hat{\theta}$	$\hat{\beta}$
Unit A	0.529	0.712	0.261	0.435
Unit B	0.705	0.818	0.328	0.506
Unit C	1.371	0.816	0.549	0.529

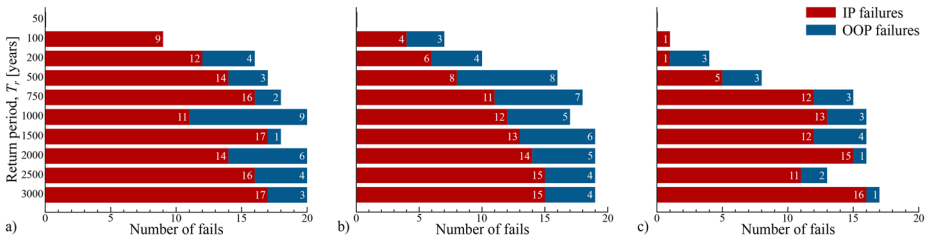


Fig. 7 Distribution of IP and OOP failure mechanisms for (**a**) Unit A, (**b**) Unit B, and (**c**) Unit C across various seismic intensity levels

Fig. 7 shows the distribution of failure mechanisms for the three isolated structural units across a range of seismic intensities. A consistent trend is observed across all three units: as the GM intensity increases, the number of IP failures rises, while the occurrence of OOP failures remains relatively constant. Therefore, at lower intensities, OOP failures represent a significant, and often dominant, failure mechanism; conversely, as the intensity of the GM increases, IP failures become progressively more dominant, accounting for most of the collapses at high seismic intensities. This suggests that local wall stability (OOP) governs the collapse at low intensities, while global capacity (IP) controls the performance under large events. Additionally, Unit A shows more OOP failures at all intensities compared to Unit C. This indicates that the increased axial load on the transverse walls, due to the larger floors, improves their local stability, effectively reducing OOP failures in these walls. Furthermore,

most of the failures occurred in the second story, which is consistent with findings in previous literature.

The analysis of the isolated structural units, which serve as the benchmark for evaluating the pounding effect, emphasizes the critical influence of OOP behavior on the overall response of URM buildings. This local behavior modifies the dynamic response by introducing higher vibration modes into the global response. These complex dynamics highlight the limitations of static analyses in capturing the actual seismic capacity and accurately determining the seismic fragility, given that the OOP mechanism accounts for a significant proportion of failures. Furthermore, the distribution of failure mechanisms across different seismic intensities reveals a complex interaction between IP and OOP responses, demonstrating that they cannot be studied independently, as has often been done in previous literature. Thus, explicitly including the OOP behavior in the numerical model is essential for an accurate seismic performance assessment of these structures.

5.2 Two-unit clusters

The pounding effect is first evaluated using configurations with two units arranged in a row, a common arrangement in many historic urban centers. Three clusters were generated by combining the structurally distinct units and denoted as AG_{xy}, where x and y correspond to the identifiers of the first and second units, respectively.

Fig. 8 presents the fragility functions for each unit within the three two-unit clusters. In AG_{AB}, the fragility curves for Unit A and Unit B are nearly identical, aligning closely with the fragility curve of the isolated Unit B. Conversely, the structural units in the remaining two clusters show distinct fragilities. In AG_{AC}, although Unit A remains more vulnerable than Unit C, its fragility curve shifted significantly to the right relative to its isolated case (indicating improved behavior), while the curve for Unit C shifts to the left (indicating deterioration). A similar trend is observed in the AG_{CB} configuration. Unit B improves its performance, but the inter-building interaction is detrimental to Unit C. These results demonstrate a consistent and dualistic impact of the pounding effect. A beneficial consequence is observed for the weaker unit, whose seismic performance is enhanced due to the kinematic constraints and support provided by the more robust adjacent structure. This support effec-

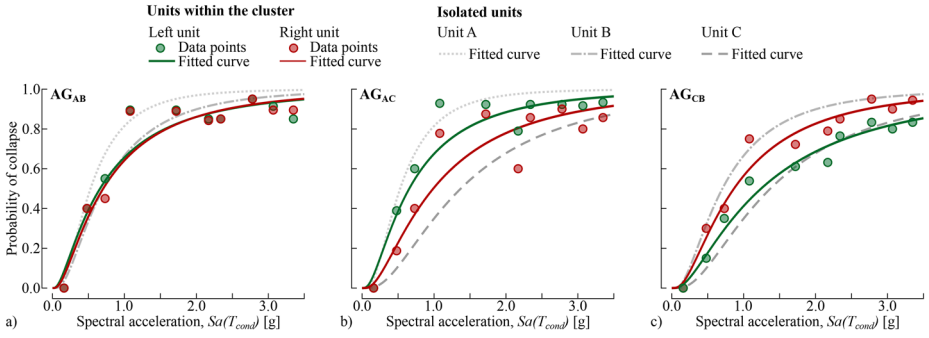


Fig. 8 Fragility functions for collapse of the structural units in two-unit clusters: (**a**) AG_{AB}, (**b**) AG_{AC}, and (**c**) AG_{CB}. Structural units within the clusters are enumerated from left to right. Dashed lines represent fragility curves of isolated units, while solid lines indicate the fragility curves of the units as part of a cluster

tively reduces its seismic vulnerability compared to its isolated condition. Conversely, this interaction has a detrimental impact on the stronger unit. Seismic pounding and the demand to support the more flexible neighbor increase the internal forces, leading to an increased probability of collapse and, thus, higher seismic fragility. Furthermore, the severity of this detrimental effect on the stronger unit depends on the initial difference in capacity between the two units; the larger the discrepancy in their isolated fragilities, the more pronounced the consequences of the pounding are for the stronger unit. Additionally, a critical shift in the governing failure mechanisms is observed when comparing the assemblies to the isolated units. While the isolated structures exhibited a significant proportion of out-of-plane (OOP) failures at lower seismic intensities (as detailed in Fig. 7), the failure mechanisms within the assembly configurations are predominantly driven by in-plane (IP) failures. Because the seismic demand is applied in the longitudinal direction, parallel to the building façades, the inter-building pounding exacerbates the shear and flexural (IP) demands on the main load-bearing walls. Simultaneously, the physical adjacency of the neighboring buildings provides a kinematic constraint that stabilizes the transverse walls against OOP instability, effectively suppressing the OOP collapse mechanisms that were prevalent in the isolated condition.

To further analyze the pounding effect, the failure sequence of the units is presented in Fig. 9, illustrating scenarios where either a single unit or both structural units collapse. The results show that the weaker unit within the clusters tends to fail first. This trend is more evident in configurations with large capacity differences: in AG_{AB}, the weaker unit (Unit A) fails at 77.8% of the single-unit failures and is the first in failing with 56.3% in the two-unit collapse scenarios; in AG_{CB}, the weaker unit (Unit B) fails first in 96.7% and 77.1% of the single- and two-unit failure cases, respectively; similarly, in AG_{AC}, the weaker unit (Unit A) represents 98.2% of the single-unit failures and initiates 84.0% of the double fail failures.

Consequently, global collapse is typically triggered by the most vulnerable unit, whose failure can subsequently induce a progressive collapse mechanism in the adjacent structures. This rationale explains the detrimental impact of the pounding effect on the stronger unit, whose own collapse is often a direct consequence of its interaction with the failing neighboring building.

To assess the interaction between adjacent buildings with different capacities, Fig. 10 presents the ratio of the pounding forces developed in AG_{AC} and AG_{CB} relative to those in

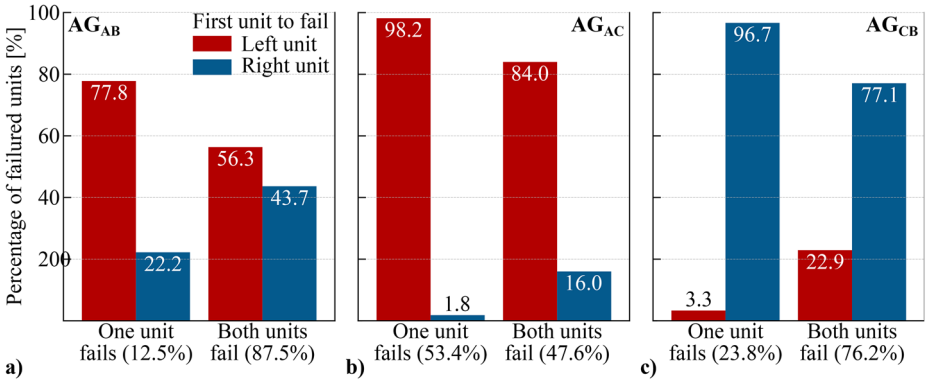


Fig. 9 Sequence of failures for the structural units within two-unit pounding: (**a**) AG_{AB}, (**b**) AG_{AC}, and (**c**) AG_{CB}

AG_{AB}. The boxplots display these impact force ratios at four distinct contact points along the height of the adjacent walls, as well as for the total pounding force. To avoid spurious values resulting from failure mechanisms, only the results from ground motions that did not induce collapse were considered. As expected, the results indicate that the pounding forces increase as the stiffness discrepancy between the units grows. For both AG_{AC} and AG_{CB} , the median impact force ratios are consistently larger than 1.0, signifying more severe impacts than in the more homogeneous AG_{AB} cluster. This effect is more evident in AG_{AC} , which pairs the stiffest unit (Unit C) with the most flexible (Unit A), showing the highest median force ratios across all contact points. Furthermore, the largest force amplifications are observed at the lower contact points, with the relative increase diminishing as the height increases. This analysis quantitatively supports the assertion that larger differences in the dynamic properties of adjacent URM buildings lead to more severe structural pounding, which in turn explains the increased fragility observed in the stronger units. Therefore, the pounding effect proves detrimental to a more resistant building when it is located adjacent to a significantly more flexible structure. However, this trend likely reaches a theoretical asymptote. If the difference in stiffness and capacity were to increase significantly beyond the archetypes studied here, the stronger unit would eventually behave as a quasi-rigid boundary for the weaker unit. In such an extreme scenario, the kinetic energy transferred from the significantly more flexible building would become negligible relative to the stronger unit's total capacity. Consequently, the detrimental effect would theoretically vanish, as the stronger structure would become effectively "decoupled" from the dynamic influence of its neighbor.

5.3 Three-unit clusters

The study is extended to more complex three-unit configurations to explore the influence of the position of each structural unit in the cluster (exterior versus interior) and the confinement effect provided by having two neighbors. The cluster configurations were specifically selected to evaluate the seismic performance of a building when it is situated between two weaker or two stronger structures, providing deeper insight into the nuanced effects of

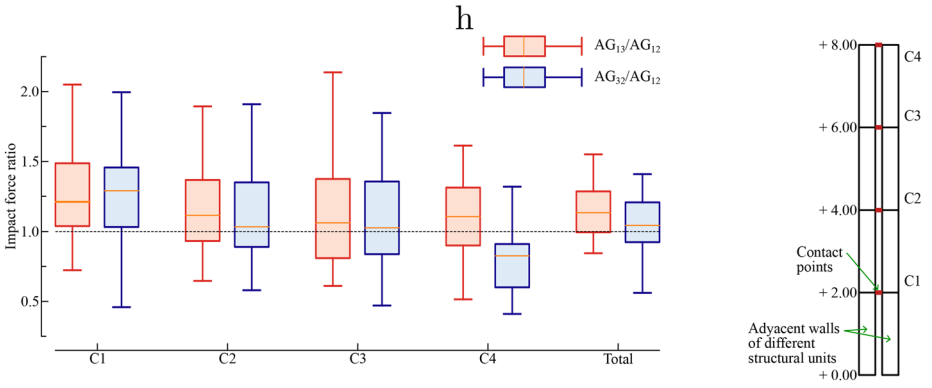


Fig. 10 Comparison of impact forces between adjacent units. The boxplots show the ratio of the forces in AG_{AC} and AG_{CB} relative to those in AG_{AB}

structural interaction within a row of buildings. Furthermore, the magnitude of the stiffness disparity between the units is also evaluated.

Fig. 11 presents the fragility curves for each building within the four different three-unit cluster configurations. Given the symmetry of the arrangements, the plots display two distinct curves for the buildings in the cluster: one representing the central unit and another representing the exterior units. The curves of the isolated units are also included for comparison purposes. Notice the absence of a uniform trend across all configurations, demonstrating that the impact of the pounding depends on the specific configuration. In AG_{ABA}, the behavior of all three units is improved by the pounding effect. The fragility functions of the external and central units are nearly identical and align closely with the curve of the stronger unit in isolation. This result aligns with the findings observed in the two-unit configuration (see results for AG_{AB}). In AG_{ACA}, the exterior units show negligible differences relative to the isolated scenario, whereas the central unit increases the fragility. These two clusters, AG_{ABA} and AG_{ACA}, have weak units in the exterior positions and a strong unit in the center, but the outcome differs due to the magnitude of the stiffness differences. In AG_{CAC}, the pounding is detrimental to all three structural units, whereas in AG_{CBC}, the pounding is beneficial for all three structural units. In AG_{CAC} and AG_{CBC}, the ponding effect varies depending on the disparity in stiffness. Thus, the differences in stiffness between adjacent URM buildings have a major impact on the overall pounding effect. Consistent with the two-unit configurations, the failure mechanisms in these three-unit assemblies are governed by IP modes (shear and flexural), as the presence of neighbors on one or both sides provides the necessary kinematic constraint to prevent OOP instability of the transverse walls.

Fig. 12 provides insight into the failure sequence of the three-unit clusters, illustrating which unit (exterior or interior) is the first to collapse. In configurations where a stronger unit is placed in the center (AG_{ABA} and AG_{ACA}), the initial failure overwhelmingly occurs

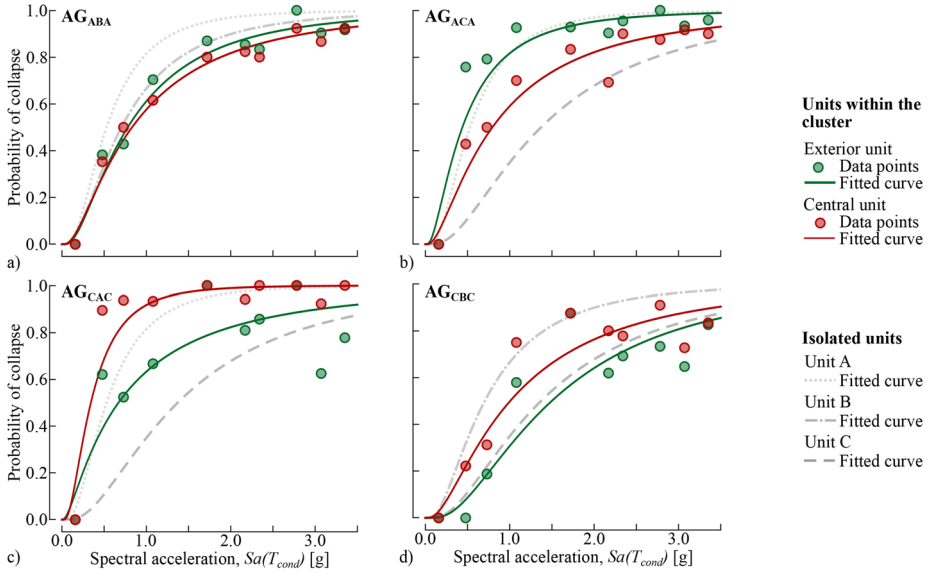


Fig. 11 Fragility functions for collapse of the structural units in three-unit clusters: **a)** AG_{ABA}, **b)** AG_{ACA}, **c)** AG_{CAC}, and **d)** AG_{CBC}. Dashed lines represent fragility curves of isolated units, while solid lines refer to fragility curves of the units as part of a cluster

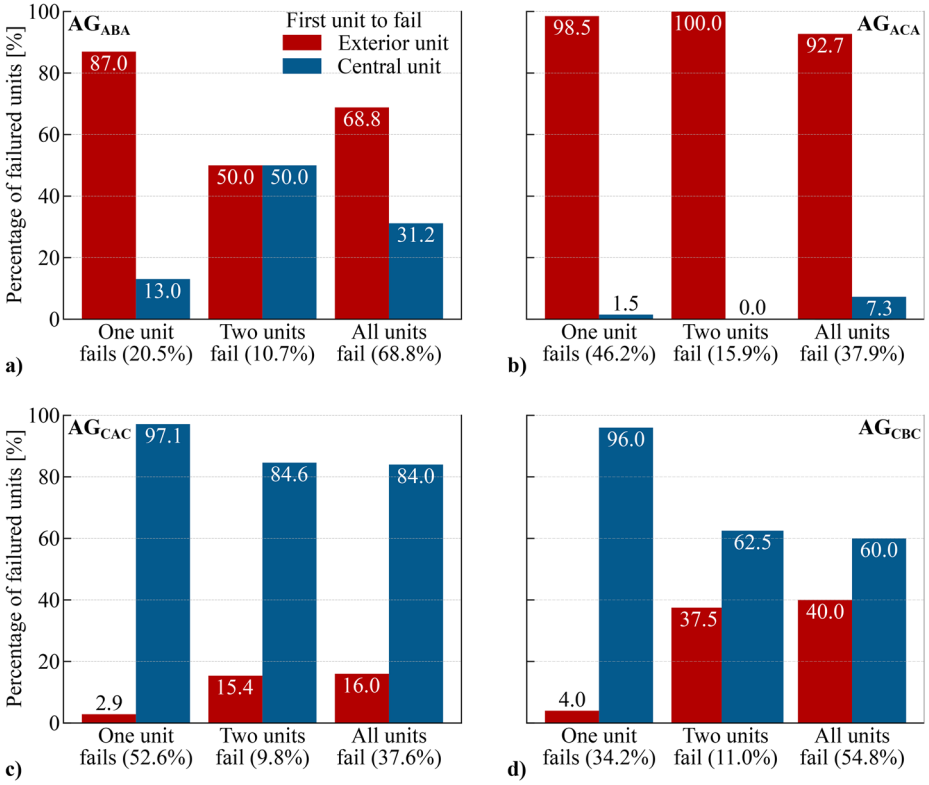


Fig. 12 Sequence of failure for the structural units within three-unit clusters: (**a**) AG_{ABA}, (**b**) AG_{ACA}, (**c**) AG_{CAC}, and (**d**) AG_{CBC}

in one of the weaker exterior units. Conversely, when a weaker unit is confined between two stronger ones (AG_{CAC} and AG_{CBC}), the central unit consistently fails first. This analysis shows that the most vulnerable building in the cluster, whether it is in an exterior or a confined central position, dictates the initiation of the collapse sequence for the entire structural system. Ultimately, these findings across both two- and three-unit configurations highlight that the pounding effect cannot be generalized as strictly beneficial or detrimental; rather, it is a highly sensitive dynamic interaction governed by the relative stiffness and position of the constituent buildings within the cluster.

Ultimately, the three-unit cluster analysis transforms the building row from a collection of isolated structures into a singular, interdependent system. The results demonstrate that the cluster's global fragility is not an average of its parts, but is dictated by its most vulnerable link. Whether the weak unit is an exterior or a confined structure, its failure initiates a progressive collapse mechanism that can prematurely exhaust the capacity of significantly stronger adjacent structures.

6 Conclusions and final remarks

This research quantified the impact of pounding on the seismic fragility of URM buildings within clusters by analyzing two-unit and three-unit configurations, which were assembled from three structural units developed with different stiffness and in-plane capacities. The units were assembled in a row, which is typical in historic urban centers, and the main interaction was pounding. The numerical modeling included in-plane and out-of-plane behaviors of the masonry elements, allowing a holistic evaluation of the URM buildings and clusters.

The analysis of the isolated structural units reveals that their dynamic response is highly complex and significantly affected by local vibration modes. This complexity is evidenced by the non-coincidence of the maximum base shear and maximum rooftop displacement, which is due to higher vibration modes affecting the translational response of the structure. These local modes of high frequencies are primarily driven by the out-of-plane behavior of the masonry walls. The critical role of this mechanism is further highlighted by the observed failure modes. Therefore, an accurate seismic performance assessment needs advanced models that can capture these complex three-dimensional effects, including in-plane and out-of-plane behaviors.

The analysis of two-unit clusters shows interesting interactions between neighboring buildings and a dichotomous effect depending on the heterogeneity of the structural units. The pounding effect for this configuration is always beneficial for the weaker building, whose seismic performance and fragility are improved due to the support provided by its neighbor. Conversely, the effect on the stronger building could be detrimental if the difference in stiffness between the two units is large. Critically, the collapse sequence is almost always initiated by the weaker unit, which fails first, even if the stronger unit eventually collapses as well. The pounding forces increase as the disparity between the stiffness of the structural units and the failure of the first unit triggers a premature failure of the second.

The analysis of the three-unit clusters highlights the impact of the heterogeneity in rows of URM buildings. Clusters with a homogeneous composition improve the behavior of the structural units relative to the case of isolated buildings, but the pounding effect becomes detrimental as the differences in stiffness and capacity increase. Additionally, the collapse sequence observed in the two-unit clusters is confirmed, the most vulnerable unit being the first to fail, regardless of its position. When a weaker unit is confined between two stronger ones, it becomes the clear point of failure for the entire system, a fact confirmed by both the failure order analysis and its significantly higher fragility compared to its neighbors. Conversely, when a stronger building is centered between two weaker ones, the failure is still initiated by one of the weaker corner units. This demonstrates that the presence of a single, more vulnerable structure can determine the failure initiation point for the entire cluster, potentially triggering a progressive collapse that compromises the stability of adjacent structures.

Previous studies have presented some contradictory results about the inter-building interaction, discussing whether it is beneficial or detrimental. However, the outcome depends on the specific configuration of the cluster, with the existence of a critical heterogeneity threshold. Homogeneous clusters (below the heterogeneity threshold) improve the behavior of the structural units relative to their isolated response, and worsen as the heterogeneity increases above this threshold. Additionally, the failure mechanisms and collapse sequences identified herein underscore the need for holistic cluster-level risk assessments, including

three-dimensional models with explicit IP-OOP coupling to capture the local behavior of masonry walls. For the clusters, the most vulnerable building, regardless of its position (exterior or confined), controls the collapse initiation for the entire structural system. This means that retrofitting a single weak building in a row can significantly improve the resilience of its neighbors, making cluster-based retrofitting more cost-effective than individual building interventions. Ultimately, this methodology allows us to identify and quantify the 'dual' effect of the building interaction: while a weaker building physically benefits from the kinematic support of a stronger neighbor, the resulting pounding interaction introduces a detrimental demand on the stronger unit. By providing quantitative evidence that the most vulnerable building triggers the progressive collapse sequence of the entire row, this work proves that isolated building assessments are unconservative, which is a critical aspect necessary for developing realistic, cluster-based seismic risk models for historic urban centers.

The present study provides fundamental insights into the pounding effect between adjacent unreinforced masonry buildings; however, the numerical models are constrained by specific geometric assumptions adopted to limit sources of uncertainty. These include equal story heights, identical unit depths, a uniform number of stories among adjacent units, and a constant floor layout direction. Therefore, future research should first study the impact of varying these geometric parameters, study asymmetrical structural units, and incorporate both horizontal components and the vertical component of the ground motions. Subsequently, this methodology can be extended to larger urban building stocks and investigate the efficacy of retrofitting strategies applied not to single buildings, but to entire building clusters. Such efforts will be indispensable for improving the resilience of historic urban centers and protecting cultural heritage against future seismic events.

Author contributions Jose A. Gallardo: Conceptualization, Methodology, Data collection, Software, Validation, Investigation, Visualization, Writing - Original Draft, Writing - Review & Editing. Igor Tomić: Conceptualization, Methodology, Software, Writing - Original Draft, Writing - Review & Editing. Nuria C. Palazzi: Data collection, Visualization, Writing - Original Draft, Writing - Review & Editing. Juan C. de la Llera: Conceptualization, Writing - Review & Editing. Katrin Beyer: Conceptualization, Methodology, Writing - Review & Editing.

Funding This research has been sponsored by the Earthquake Engineering and Structural Dynamics (EESD) laboratory at EPFL, Switzerland, and ANID, under the ANID/doctorate scholarship/21201370; Research Center for Integrated Disaster Risk Management (CIGIDEN), ANID/FONDAP/1523A0009; and FONDECYT project, Multi-scale earthquake risk mitigation of healthcare networks using seismic isolation, ANID/FONDECYT/1220292. The third author acknowledges financial support from ANID/FONDECYT Regular 1261104. The authors are grateful for all this support.

Data availability The datasets generated during and/or analyzed during the current study are available from the corresponding author on reasonable request.

Declarations

Competing interest The authors declare that they have no known competing financial interests or personal relationships that could have appeared to influence the work reported in this paper.

References

Almeida JP, Beyer K, Brunner R, Wenk T (2020) Characterization of mortar–timber and timber–timber cyclic friction in timber floor connections of masonry buildings. Mater Struct 53(3). https://doi.org/10.1617/s11527-020-01483-y

AlShawa O, Liberatore D, Sorrentino L (2024) Pre-and post-simulations of shake-table tests on a stone masonry building aggregate using finite-discrete elements. Bull Earthq Eng 22(12):6093–6121. https://doi.org/10.1007/s10518-022-01550-5

Angiolilli M, Brunelli A, Cattari S (2023) Fragility curves of masonry buildings in aggregate accounting for local mechanisms and site effects. Bull Earthq Eng 21:2877–2919. https://doi.org/10.1007/s10518-023-01635-9

Angiolilli M, Lagomarsino S, Cattari S, Degli Abbati S (2021) Seismic fragility assessment of existing masonry buildings in aggregate. Eng Struct 247:113218. https://doi.org/10.1016/j.engstruct.2021.113218

Aşıkoğlu A, D'anna J, Ramirez R, Solarino F, Romanazzi A, Ciocci MP, Bianchini N (2024) Simulation of blind pre-diction and post-diction shaking table tests on a masonry building aggregate using a continuum modelling approach. Bull Earthq Eng 22(12):6163–6193. https://doi.org/10.1007/s10518-023-01666-2

Atalić J, Demšić M, Baniček M et al (2023) The December 2020 magnitude ($\mathbf{M}_{\mathbf{w}}$) 6.4 Petrinja earthquake, Croatia: seismological aspects, emergency response and impacts. Bull Earthq Eng 21(13):5767–5808. https://doi.org/10.1007/s10518-023-01758-z

Atalić J, Uroš M, Šavor Novak M, Demšić M, Nastev M (2021) The $\mathbf{M}_{\mathbf{w}}$ 5. 4 Zagreb (croatia) earthquake of March 22, 2020: impacts and response. Bull Earthq Eng 19(9):3461–3489. https://doi.org/10.1007/s10518-021-01117-w

Baker JW (2015) Efficient analytical fragility function fitting using dynamic structural analysis. Earthquake Spectra 31(1):579–599. https://doi.org/10.1193/021113EQS025M

Baquedano-Juliá P, Ferreira TM, Arriagada-Luco C, Sandoval C, Palazzi NC, Oliveira DV (2024) Multi-vulnerability analysis for seismic risk management in historic city centres: an application to the historic city centre of La Serena, Chile. Nat Hazards 120(10):9223–9266. https://doi.org/10.1007/s11069-023-06008-8

Bernardini C, Maio R, Boschi S, Ferreira TM, Vicente R, Vignoli A (2019) The seismic performance-based assessment of a masonry building enclosed in aggregate in Faro (portugal) by means of a new target structural unit approach. Eng Struct 191:386–400. https://doi.org/10.1016/j.engstruct.2019.04.040

Bianchini N, Ciocci M, Solarino F, Romanazzi A, Ramirez R, D'anna J, Aşıkoğlu A (2024) Influence of wall-to-floor connections and pounding on pre-and post-diction simulations of a masonry building aggregate tested on a shaking table. Bull Earthq Eng 22(12):6141–6161. https://doi.org/10.1007/s10518-023-01641-x

Brignola A, Podestä S, Pampanin S (2008) In-plane stiffness of wooden floor. In 2008 New Zealand Society of Earthquake Engineering (NZSEE) Conference

Candia G, Macedo J, Jaimes MA, Magna-Verdugo C (2019) A new state-of-the-art platform for probabilistic and deterministic seismic hazard assessment. Seismolog Res Lett 90(6):2262–2275. https://doi.org/10.1785/0220190025

Carocci CF (2012) Small centres damaged by 2009 L'Aquila earthquake: on site analyses of historical masonry aggregates. Bull Earthq Eng 10(1):45–71. https://doi.org/10.1007/s10518-011-9284-0

Castro S, Benavente R, Crempien JGF, Candia G, de la Llera JC (2022) A consistently processed strong-motion database for Chilean earthquakes. Seismolog Res Lett 93(5):2700–2718. https://doi.org/10.1785/0220200336

Cattari S, Alfano S, Lagomarsino S (2023) A practice-oriented proposal to consider the flange effect in equivalent frame modeling of masonry buildings. Buildings 13(2):462. https://doi.org/10.3390/buildings13020462

D'Altri AM, Sarhosis V, Milani G, Rots J, Cattari S, Lagomarsino S, Sacco E, Tralli A, Castellazzi G, de Miranda S (2020) Modeling strategies for the computational analysis of unreinforced masonry structures: review and classification. Archives Comput Methods Eng 27(4):1153–1185. https://doi.org/10.1007/s11831-019-09351-x

D'Ayala D (2013) Assessing the seismic vulnerability of masonry buildings. In: Handbook of seismic risk analysis and management of civil infrastructure systems. Elsevier, pp 334–365

D'Ayala D, Benzoni G (2012) Historic and traditional structures during the 2010 Chile earthquake: observations, codes, and conservation strategies. Earthquake Spectra 28(1_suppl1):425–451. https://doi.org/10.1193/1.4000030

D'Ayala D, Speranza E (2003) Definition of collapse mechanisms and seismic vulnerability of historic masonry buildings. Earthquake Spectra 19(3):479–509. https://doi.org/10.1193/1.1599896

Da Porto F, Munari M, Prota A, Modena C (2013) Analysis and repair of clustered buildings: case study of a block in the historic city centre of L'Aquila (Central Italy). Construct Building Mater 38:1221–1237. https://doi.org/10.1016/j.conbuildmat.2012.09.108

Di Trapani F, Villar S, Di Benedetto M, Petracca M, Camata G (2024) Seismic response of unreinforced masonry building aggregates: investigation on the "aggregate-effect" based on an elementary building aggregate. Eng Struct 316:118301. https://doi.org/10.1016/j.engstruct.2024.118301

FEMA (2020) Hazus earthquake Model. Technical manual. Federal Emergency Management Agency. Washington, D.C. https://fema.gov

Fiorentino G, Forte A, Pagano E, Sabetta F, Baggio C, Lavorato D, Nuti C, Santini S (2018) Damage patterns in the town of Amatrice after August 24th 2016 central Italy earthquakes. Bull Earthq Eng 16(3):1399–1423. https://doi.org/10.1007/s10518-017-0254-z

Formisano A, Florio G, Landolfo R, Mazzolani FM (2015) Numerical calibration of an easy method for seismic behaviour assessment on large scale of masonry building aggregates. Adv Eng Softw 80:116–138. https://doi.org/10.1016/j.advengsoft.2014.09.013

Formisano A, Massimilla A (2018) A novel procedure for simplified nonlinear numerical modeling of structural units in masonry aggregates. Int J Architectural Heritage 12(7–8):1162–1170. https://doi.org/10.1080/15583058.2018.1503365

Gagliardo R, Godio M, Portioli FP, Landolfo R (2024) Seismic analysis of failure mechanisms in adjacent interacting stone masonry buildings via rigid block modeling. Bull Earthq Eng 22(12):6195–6224. https://doi.org/10.1007/s10518-023-01659-1

Galvez F, Dizhur D, Ingham J (2024) Adjacent interacting masonry structures: shake table test blind prediction discrete element method simulation. Bull Earthq Eng 22(12):6037–6063. https://doi.org/10.1007/s10518-023-01640-y

Goldsmith W (1960) Contact phenomena produced by the impact of elastic bodies. Impact: Theory Phys Behav Colliding Solids

Greco A, Lombardo G, Pantò B, Famà A (2020) Seismic vulnerability of historical masonry aggregate buildings in oriental Sicily. Int J Architectural Heritage 14(4):517–540. https://doi.org/10.1080/15583058.2018.1553075

Guerrini G, Senaldi I, Graziotti F, Magenes G, Beyer K, Penna A (2019) Shake-table test of a strengthened stone masonry building aggregate with flexible diaphragms. Int J Architectural Heritage 13(7):1078–1097. https://doi.org/10.1080/15583058.2019.1635661

Hughes PJ, Mosqueda G (2020) Evaluation of uniaxial contact models for moat wall pounding simulations. Earthquake Eng Struct Dyn 49(12):1197–1215. https://doi.org/10.1002/eqe.3285

Indirli M, Kouris LAS, Formisano A, Borg RP, Mazzolani FM (2013) Seismic damage assessment of unreinforced masonry structures after the abruzzo 2009 earthquake: the case study of the historical centers of L'Aquila and Castelvecchio Subequo. Int J Architectural Heritage 7(5):536–578. https://doi.org/10.1080/15583058.2011.654050

INN (1996) NCh433: Earthquake resistant design of buildings (in Spanish). Instituto Nacional de Normalización (INN). Santiago, Chile

INN (2020) NCh3389: structure - seismic stabilizaton of historical and existing buildings - requirements for the structural design (in Spanish). Instituto Nacional de Normalización (INN), Santiago, Chile

Ismail N, Khattak N (2019) Observed failure modes of unreinforced masonry buildings during the 2015 hindu kush earthquake. Earthquake Eng Eng Vibr 18(2):301–314. https://doi.org/10.1007/s11803-019-0505-x

Jayaram N, Lin T, Baker JW (2011) A computationally efficient ground-motion selection algorithm for matching a target response spectrum mean and variance. Earthquake Spectra 27(3):797–815. https://doi.org/10.1193/1.3608002

Jorquera-Silva N (2017) Culturas constructivas que conforman el patrimonio Chileno construido en tierra (in Spanish). AUS - Arquitectura / Urbanismo / Sustentabilidad (16):30–35:30–35. https://doi.org/10.4206/aus.2014.n16-06

Malomo D, DeJong M (2024) M-dem simulation of seismic pounding between adjacent masonry structures. Bull Earthq Eng 22(12):6067–6092. https://doi.org/10.1007/s10518-022-01545-2

McKenna F, Fenves GL, Scott MH et al (2000) Open system for earthquake engineering simulation. University of California, Berkeley, CA

Muñoz JP, D'Ayala D, Palazzi NC et al. (2025) A new procedure to derive typological fragility functions for unreinforced masonry structures: an application to a Chilean case. Bull Earthq Eng. https://doi.org/10.1007/s10518-025-02190-1

Çetin ÖK, Bray JD, Frost JD et al (2023 February 6, 2023. Türkiye earthquakes: report on geoscience and engineering impacts. Tech. rep., Geotechnical extreme event reconnaissance association (GEER), the earthquake engineering research institute, and the earthquake engineering foundation of Türkiye. GEER association report 082. https://doi.org/10.18118/G6PM34

Palazzi NC, Barrientos M, Sandoval C, de la Llera JC (2023) Seismic vulnerability assessment of the Yungay's historic urban center in Santiago, Chile. J Eart Eng 27(7):1821–1848. https://doi.org/10.1080/13632469.2022.2087793

Penna A, Morandi P, Rota M, Manzini CF, da Porto F, Magenes G (2014) Performance of masonry buildings during the emilia 2012 earthquake. Bull Earthq Eng 12(5):2255–2273. https://doi.org/10.1007/s10518-013-9496-6

Pnevmatikos N, Konstandakopoulou F, Koumoutsos N (2020) Seismic vulnerability assessment and loss estimation in Cephalonia and Ithaca islands, Greece, due to earthquake events: a case study. Soil Dyn Earthquake Eng 136:106252. https://doi.org/10.1016/j.soildyn.2020.106252

Quagliarini E, Maracchini G, Clementi F (2017) Uses and limits of the equivalent frame model on existing unreinforced masonry buildings for assessing their seismic risk: a review. J Building Eng 10:166–182. https://doi.org/10.1016/j.jobe.2017.03.004

Ramaglia G, Lignola GP, Prota A (2024) Preliminary nonlinear analysis of a scaled masonry building under shaking test for the blind prediction of the SERA AIMS project. Bull Earthq Eng 22(12):6123–6140. https://doi.org/10.1007/s10518-023-01639-5

Reddy JN (2014) An introduction to nonlinear finite element analysis: with applications to heat transfer, fluid mechanics, and solid mechanics. Oxford University Press. https://doi.org/10.1093/acprof:oso/9780199641758.001.0001

Ross RJ (2010) Wood handbook: wood as an engineering material, centennial edn. U.S. Department of Agriculture, Forest Products Laboratory, Forest Service. https://doi.org/10.2737/FPL-GTR-190

Ruggieri S, Liguori FS, Leggieri V, Bilotta A, Madeo A, Casolo S, Uva G (2023) An archetype-based automated procedure to derive global-local seismic fragility of masonry building aggregates: META-FORMA-XL. Int J Disaster Risk Reduct 95:103903. doi: 103903. https://doi.org/10.1016/j.ijdrr.2023.103903

Salazar F, Gerardo L, Ferreira TM (2020) Seismic vulnerability assessment of historic constructions in the downtown of Mexico city. Sustainability 12(3):1276. https://doi.org/10.3390/su12031276

Senaldi IE, Guerrini G, Comini P, Graziotti F, Penna A, Beyer K, Magenes G (2020) Experimental seismic performance of a half-scale stone masonry building aggregate. Bull Earthq Eng 18(2):609–643. https://doi.org/10.1007/s10518-019-00631-2

Shabani A, Kioumarsi M, Zucconi M (2021) State of the art of simplified analytical methods for seismic vulnerability assessment of unreinforced masonry buildings. Eng Struct 239:112280. https://doi.org/10.1016/j.engstruct.2021.112280

Shrestha B, Hao H (2018) Building pounding damages observed during the 2015 gorkha earthquake. J Perform Constr Facil 32(2):04018006. https://doi.org/10.1061/(ASCE)CF.1943-5509.0001134

Tomazevic M (1999) Earthquake-resistant design of masonry buildings, vol 1. World Scientific

Tomić I, Beyer K (2024) Shake-table test on a historical masonry aggregate: prediction and postdiction using an equivalent-frame model. Bull Earthq Eng 22(12):6225–6258. https://doi.org/10.1007/s10518-023-01765-0

Tomić I, Penna A, DeJong M, Butenweg C, Correia AA, Candeias PX, Senaldi I, Guerrini G, Malomo D, Beyer K (2024a) Shake table testing of a half-scale stone masonry building aggregate. Bull Earthq Eng 22(12):5963–5991. https://doi.org/10.1007/s10518-023-01810-y

Tomić I, Penna A, DeJong M, Butenweg C, Correia AA, Candeias PX, Senaldi I, Guerrini G, Malomo D, Wilding B, Pettinga D, Spanenburg M, Galanakis N, Oliver S, Parisse F, Marques R, Cattari S, Lourenço PB, Galvez F, Dizhur D, Ingham JM, Ramaglia G, Lignola GP, Prota A, AlShawa O, Liberatore D, Sorrentino L, Gagliardo R, Godio M, Portioli F, Landolfo R, Solarino F, Bianchini N, Ciocci MP, Romanazzi A, Aşıkoğlu A, D'anna J, Ramirez R, Romis F, Marinković M et al (2024b) Shake-table testing of a stone masonry building aggregate: overview of blind prediction study. Bull Earthq Eng 22(12):5993–6035. https://doi.org/10.1007/s10518-022-01582-x

Tomić I, Vanin F, Beyer K (2021) Uncertainties in the seismic assessment of historical masonry buildings. Appl Sci 11(5):2280. https://doi.org/10.3390/app11052280

UNDRR (2019) Global assessment report on disaster risk reduction 2019. United Nations Office for Disaster Risk Reduction (UNDRR)

Uroš M, Atalić J, Demšić M, Baniček M, Šavor-Novak M, Kadić A (2024) Impact of devastating earthquakes in Croatia in 2020. J Appl Eng Sci 22(2):239–244. https://doi.org/10.5937/jaes0-50405

Vanin F, Penna A, Beyer K (2020a) Equivalent-frame modeling of two shaking table tests of masonry buildings accounting for their out-of-plane response. Front Built Environ 6. https://doi.org/10.3389/fbuil.2020.00042

Vanin F, Penna A, Beyer K (2020b) A three-dimensional macroelement for modelling the in-plane and out-of-plane response of masonry walls. Earthquake Eng Struct Dyn 49(14):1365–1387. https://doi.org/10.1002/eqe.3277

Publisher's Note Springer Nature remains neutral with regard to jurisdictional claims in published maps and institutional affiliations.

Springer Nature or its licensor (e.g. a society or other partner) holds exclusive rights to this article under a publishing agreement with the author(s) or other rightsholder(s); author self-archiving of the accepted manuscript version of this article is solely governed by the terms of such publishing agreement and applicable law.

Authors and Affiliations

José A. Gallardo[1,2] · Igor Tomić[3] · Nuria C. Palazzi[2,4] · Juan C. de la Llera[1,2] · Katrin Beyer[3]

✉ José A. Gallardo
jogallardo@uc.cl

Igor Tomić
igor.tomic@epfl.ch

Nuria C. Palazzi
nuria.palazzi@unab.cl

Juan C. de la Llera
jcllera@ing.puc.cl

Katrin Beyer
katrin.beyer@epfl.ch

[1] Department of Structural and Geotechnical Engineering, Pontificia Universidad Católica de Chile, Santiago, Chile

[2] Research Center for Integrated Disaster Risk Management (CIGIDEN), Santiago, Chile

[3] Earthquake Engineering and Structural Dynamics Laboratory (EESD), School of Architecture, Civil and Environmental Engineering (ENAC), École Polytechnique Fédérale de Lausanne (EPFL), Lausanne, Switzerland

[4] Faculty of Architecture, Art, Design and Communications, Universidad Andrés Bello, Santiago, Chile